nuclear fusion
IAEA

PAPER • OPEN ACCESS

An analytical model for two-step reaction gamma-ray spectroscopy in magnetized plasmas

To cite this article: A. Valentini *et al* 2025 *Nucl. Fusion* **65** 046031

OPEN ACCESS
IOP Publishing | International Atomic Energy Agency
Nuclear Fusion
Nucl. Fusion **65** (2025) 046031 (14pp)
https://doi.org/10.1088/1741-4326/adc1df

An analytical model for two-step reaction gamma-ray spectroscopy in magnetized plasmas

A. Valentini[1,2], B.C.G. Reman[1,3], M. Nocente[2,*], J. Eriksson[5], H. Järleblad[4], D. Moseev[6], M. Rud[1], A. Snicker[7] and M. Salewski[1]

[1] Department of Physics, Technical University of Denmark, 2800 Kgs. Lyngby, Denmark
[2] Department of Physics, University of Milano-Bicocca, 20126 Milan, Italy
[3] Laboratory for Plasma Physics LPP-ERM/KMS, B-1000 Brussels, Belgium
[4] Department of Appl. Math. & Computer Science, Technical University of Denmark, 2800 Kgs. Lyngby, Denmark
[5] Department of Physics and Astronomy, Uppsala University, 75120 Uppsala, Sweden
[6] Max-Planck-Institut fur Plasmaphysik, Wendelsteinstr. 1, Greifswald 17491, Germany
[7] VTT, Technical Research Centre of Finland, Espoo, Finland

E-mail: massimo.nocente@unimib.it

Received 18 December 2024, revised 3 March 2025
Accepted for publication 18 March 2025
Published 28 March 2025

Abstract

We present a method to analytically compute gamma-ray spectra generated via two-step fusion reactions, where a gamma-ray is emitted from the excited nucleus generated in the first step of the reaction. If one reactant is energetic and the other is at rest, the first step of the reaction can be treated analytically. The second step, which is the gamma-ray emission from the excited nucleus, can always be treated analytically. The model we derive is tested against the established forward-model code GENESIS, obtaining very satisfactory results. Our fully analytic treatment is a far less expensive technique than standard Monte Carlo methods, achieving several times faster computations. Fast calculations of spectra are especially beneficial when working with finely-resolved 3D-4D phase spaces. Furthermore, tractable analytical expressions give insight that is not provided by Monte Carlo methods. The formalism used for the first step of the reaction additionally allows the computation of birth distributions of fusion products from any beam-target reaction with one reactant at rest, e.g. fusion-born alpha distributions.

Keywords: fast ions, gamma-ray spectroscopy, fusion products, energy distribution, analytical model

(Some figures may appear in colour only in the online journal)

* Author to whom any correspondence should be addressed.

1. Introduction

Fast ions in present and future thermonuclear devices play a major role in heating the plasma, while also affecting the confinement of energy and of particles [1–6]. External heating mechanisms [7, 8] and fusion reactions generate energetic particles (EPs) in the keV to MeV energy range. To study the heating and any excitation of EP-driven modes, we need to know the velocity- and position-space distributions of EPs. Several codes can compute EP distribution functions by solving transport equations, semi-analytically [9] or numerically [10], or by running test-particle simulations [11, 12]. Comparisons between numerical codes and measurements [13] can be done via synthetic diagnostics, where a synthetic signal implied by a numerically computed distribution function is generated, which can be compared with the measurement. Alternatively, one can compute the phase-space sensitivity of the diagnostics [14–23] and calculate a tomographic inversion [24–30] of the measured data to directly compare with the simulation. This second way also relies on synthetic diagnostics.

Neutron emission spectroscopy (NES) and gamma-ray spectroscopy (GRS) rely on measurement of fusion products and are predicted to work best, with respect to other diagnosis techniques, in reactor-grade plasmas as they typically have high signal-to-noise ratios [13, 28, 31–33]. Fusion plasmas emit gamma rays generated either in one-step reactions or in two-step reactions [34, 35]. In one-step reactions, the gamma-ray is a direct reaction product, as for example in $\mathrm{D(p,g)^3He}$, $\mathrm{T(p,g)}\alpha$ and $\mathrm{T(D,g)^5He}$ [18, 36–38], where 'g' denotes a gamma ray. In two-step reactions, an excited nucleus is born in the fusion reaction and immediately decays emitting a gamma ray, as, for example, in $^9\mathrm{Be}(\alpha,\mathrm{ng})^{12}\mathrm{C}$ and $^{10}\mathrm{B}(\alpha,\mathrm{pg})^{13}\mathrm{C}$ [17, 34, 39–41]. In ITER, two-step GRS and collective Thomson scattering are currently the only diagnostics foreseen to measure the distribution function of confined alpha particles [31, 42, 43].

Usually, Monte Carlo techniques are used to generate synthetic NES and GRS spectra [34, 37, 44] which account for the full velocity-space distribution of both reactants, but can be computationally expensive. Recent progress allows the calculation of spectra fully analytically for beam-target one-step reactions (NES or GRS) with one fast particle ('beam') and one particle at rest ('target') in a classical [45] or a relativistic framework [46]. The advantage of an analytical treatment resides in providing further insights into the physical mechanism of spectra formation, by interpreting the single steps independently, and in the possibility of performing much faster calculations. Here, we derive an analytical model to treat the considerably more complicated two-step reactions. In one-step fusion reactions, we measure the velocity of the detected fusion product, which must be moving along the line of sight to be detected. In contrast, in two-step reactions, we measure the velocity component along the line of sight via the Doppler shift of the emitted gamma-ray, which yields far less information.

In the following, we derive the model in section 2 by solving the reaction kinematics, computing the excited product birth distribution and then calculating the gamma-ray Doppler spectrum. We further test the model validity in section 3 by comparing both steps of the reaction against Monte Carlo simulations with the GENESIS code. Finally, we discuss possible applications in section 4 and provide conclusions in section 5.

2. Analytical model

The JET tokamak was equipped with a beryllium wall, such that the best reaction to measure alpha particles is $^9\mathrm{Be}(\alpha,\mathrm{ng})^{12}\mathrm{C}$, which we can write explicitly as

$$\begin{aligned} \alpha + {}^9\mathrm{Be} &\rightarrow \mathrm{n} + {}^{12}\mathrm{C}^* \\ {}^{12}\mathrm{C}^* &\rightarrow {}^{12}\mathrm{C} + \mathrm{g}\,, \end{aligned} \tag{1}$$

where a fast alpha particle reacts with a beryllium impurity and generates a neutron and a carbon nucleus in its first excited state '1 L', which in turn emits a gamma-ray on a time scale of a picosecond [34]. In (1), the second excited state '2 L' can also be populated, but at least one order of magnitude less likely for $E_\alpha \lesssim 4\,\mathrm{MeV}$ [47, 48]. The energy released from the reaction is $Q = 5.70\,\mathrm{MeV}$, which is released in two steps. In the first step, an effective energy of $Q_{\mathrm{eff}} = 1.26\,\mathrm{MeV}$ is released and shared among the neutron and the excited carbon. In the second step, when the excited carbon decays to its ground state, a gamma-ray with energy $E_{g0} = Q - Q_{\mathrm{eff}} = 4.44\,\mathrm{MeV}$ is emitted in the rest-frame of the carbon. The detected gamma-ray is Doppler-shifted due to the motion of the excited nucleus, and in our model we implement this in the relativistic picture, also considering the aberration-of-light effect. The two-step nature of this type of measurements makes them considerably harder to interpret than one-step reaction GRS measurements, since the aim is to do inference on the fast alpha and not the excited carbon nucleus, whose velocity has a non-trivial distribution. In the following, we first study the kinematics of the two-body interaction, then calculate the birth distribution of the excited product and finally compute the gamma-ray spectrum.

2.1. Reaction kinematics

The spectrum formation in GRS is governed by energy and momentum conservation, during both steps of the reaction process. In the relativistic framework, we consider the four-momentum of a particle, which is

$$P = \left(P^0, \boldsymbol{p}\right) = \left(\frac{E_{\mathrm{tot}}}{c}, \boldsymbol{p}\right) = \left(\frac{E + mc^2}{c}, \boldsymbol{p}\right)\,, \tag{2}$$

where P^0 is the total energy E_{tot} divided by the speed of light c, $E = (\gamma - 1)mc^2$ is the relativistic kinetic energy, and $\boldsymbol{p} = \sqrt{E(E + 2mc^2)}\hat{\boldsymbol{p}}/c$ is the three-vector linear momentum of the particle. For gamma rays, the rest mass m is equal to zero. The Lorentz factor is given by $\gamma = (1 - (v/c)^2)^{-1/2}$ where v is the particle speed. We choose the time-like Minkowski metric such that the four-vector dot product reads

$$P_1 \cdot P_2 = P_1^0 P_2^0 - \boldsymbol{p}_1 \cdot \boldsymbol{p}_2\,, \tag{3}$$

which implies that the Minkowski norm of the four-momentum is the rest energy of the particle divided by c, i.e. $\sqrt{P\cdot P}=mc$. From here on, we use calligraphic font for the excited product and also drop atomic mass superscripts, i.e. $\mathfrak{C}\equiv{}^{12}\mathrm{C}^*$, in order to simplify the notation. In order to find the energy of the excited carbon, we apply four-momentum conservation to reaction (1)

$$P_\alpha + P_{\mathrm{Be}} = P_{\mathfrak{C}} + P_{\mathrm{n}}\,. \tag{4}$$

In the relativistic framework, the rest mass of the excited carbon is larger than of the ground-state carbon, i.e. $m_{\mathfrak{C}}=m_{\mathrm{C}}+E_{g0}/c^2$. In order to eliminate the neutron contribution from the balance, we isolate P_{n} and square both sides:

$$\begin{aligned}(P_{\mathrm{n}})^2 &= (P_\alpha + P_{\mathrm{Be}} - P_{\mathfrak{C}})^2 \\ &= (P_\alpha + P_{\mathrm{Be}})^2 + P_{\mathfrak{C}}^2 - 2\,(P_\alpha + P_{\mathrm{Be}})\cdot P_{\mathfrak{C}}\,.\end{aligned} \tag{5}$$

For stationary beryllium with $\boldsymbol{p}_{\mathrm{Be}}=\boldsymbol{0}$, and so $\gamma_{\mathrm{Be}}=1$, we obtain

$$\begin{aligned}m_{\mathrm{n}}^2c^2 &= (\gamma_\alpha m_\alpha c + m_{\mathrm{Be}}c, \boldsymbol{p}_\alpha)^2 + m_{\mathfrak{C}}^2c^2 \\ &\quad - 2\,(\gamma_\alpha m_\alpha c + m_{\mathrm{Be}}c, \boldsymbol{p}_\alpha)\cdot(\gamma_{\mathfrak{C}} m_{\mathfrak{C}} c, \boldsymbol{p}_{\mathfrak{C}}) \\ &= (\gamma_\alpha m_\alpha c + m_{\mathrm{Be}}c)^2 - \boldsymbol{p}_\alpha^2 + m_{\mathfrak{C}}^2c^2 \\ &\quad - 2\,(\gamma_\alpha m_\alpha c + m_{\mathrm{Be}}c)\,\gamma_{\mathfrak{C}} m_{\mathfrak{C}} c + 2\boldsymbol{p}_\alpha\cdot\boldsymbol{p}_{\mathfrak{C}}\,.\end{aligned} \tag{6}$$

The dot product of the three-momenta appearing in (6) is

$$\boldsymbol{p}_\alpha\cdot\boldsymbol{p}_{\mathfrak{C}} = |\boldsymbol{p}_\alpha||\boldsymbol{p}_{\mathfrak{C}}|\cos\theta_{\mathrm{lab}}\,, \tag{7}$$

where θ_{lab} is the emission angle of $\mathfrak{C}$ in the laboratory reference frame with respect to the alpha linear momentum. Whereas this angle can span the entire interval $[0,\pi]$ in standard reactions, for two-step reactions it can have a restricted domain. We solve equation (6) for the energy of the excited product $E_{\mathfrak{C}}$ as shown in [46]:

$$E_{\mathfrak{C}} = \frac{-\frac{\mathfrak{b}}{2} \pm \mathrm{sgn}\,(\cos\theta_{\mathrm{lab}})\sqrt{\left(\frac{\mathfrak{b}}{2}\right)^2 - \mathfrak{a}\mathfrak{c}}}{\mathfrak{a}}\,, \tag{8}$$

where

$$\begin{aligned}\mathfrak{a} &= A^2 - \frac{E_\alpha}{c^2}\left(\frac{E_\alpha}{c^2}+2m_\alpha\right)\cos^2\theta_{\mathrm{lab}}\,, \\ \mathfrak{b} &= 2\left[A\left(A\cdot m_{\mathfrak{C}}c^2 - \frac{B}{2}\right) - E_\alpha\left(\frac{E_\alpha}{c^2}+2m_\alpha\right)m_{\mathfrak{C}}\cos^2\theta_{\mathrm{lab}}\right], \\ \mathfrak{c} &= \left(A\cdot m_{\mathfrak{C}}c^2 - \frac{B}{2}\right)^2\end{aligned} \tag{9}$$

with

$$\begin{aligned}A &= \frac{E_\alpha}{c^2} + m_\alpha + m_{\mathrm{Be}}\,, \\ B &= A^2c^2 - E_\alpha\left(\frac{E_\alpha}{c^2}+2m_\alpha\right) + m_{\mathfrak{C}}^2c^2 - m_{\mathrm{n}}^2c^2\,.\end{aligned} \tag{10}$$

The $\pm$ in equation (8) corresponds to two possible solutions, which can both be physical for two-step reactions. In the Monte-Carlo approach, the sign is determined by a 50–50 chance for every event, unless the emission is sampled in the center-of-mass rest frame. For one-step reactions [45, 46], we can always discard the '−' solution on physical grounds for the usual energy ranges of fast ions in magnetized plasmas. However, for two-step reactions, the center-of-mass initial speed v_{CM} can be larger than the carbon speed in the center-of-mass frame $w_{\mathfrak{C}}$ due to the low effective energy release Q_{eff}, as depicted in figure 1. The conservation of four-momentum forbids backward emission in this case. Additionally, for a given alpha-particle energy E_α, equation (8) suggests a relationship between the excited carbon energy $E_{\mathfrak{C}}$ and the emission angle in the laboratory frame θ_{lab}, which we plot in figure 2(a) for $E_\alpha=[0.6, 1.9, 3.4]$ MeV. As it could be seen from figure 1, the larger the alpha-particle energy, the larger the minimum and maximum possible excited carbon energies, as well as a smaller maximum emission angle in the laboratory frame (corresponding to a larger cosine). Additionally, in figure 2(b) we show the center-of-mass emission angle calculated via relativistic velocity addition [46], for which $\cos\theta_{\mathrm{CM}}$ can take any value between -1 and 1.

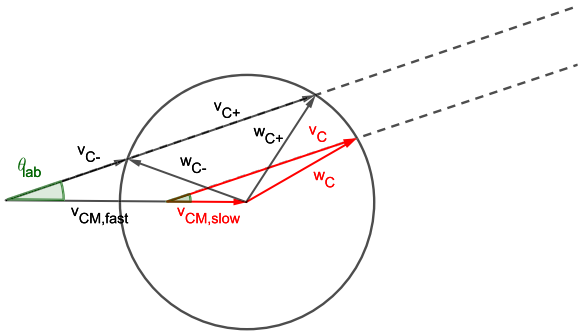

Figure 1. Classical picture of velocity addition after the reaction occurs, for a case of fast (black arrow) and slow (red arrows) center-of-mass v_{CM} with respect to the product speed in the center-of-mass rest frame, i.e. $w_{\mathfrak{C}}$. In the high-speed case, the product speed in both laboratory frame, i.e. $v_{\mathfrak{C}}$, and center-of-mass frame, i.e. $w_{\mathfrak{C}}$, have '+' and '−' solutions accordingly to equation (8). Please note that the carbon index is simply in normal font in the drawing.

The maximum emission angle (i.e. the minimum cosine value) shown in figure 2(c) can be calculated by setting the radicand in equation (8) to zero, giving

$$(\cos\theta_{\mathrm{lab}})^{\mathrm{min}} = \sqrt{\frac{A^2m_{\mathfrak{C}}^2c^4 - \frac{B^2}{4}}{E_\alpha\,(E_\alpha+2m_\alpha c^2)\,m_{\mathfrak{C}}^2}}\,. \tag{11}$$

The equation above corroborates what is shown in figure 1, namely that higher alpha particle energies E_α lead to a smaller maximum emission angle for the excited carbon in the laboratory frame. Given a stationary target beryllium, we can derive the threshold value for E_α such that the cosine in equation (11) is zero: whenever the excited carbon cannot be emitted perpendicularly, we enter the regime of backward-forbidden emission. In figure 2(c) we show how $(\cos\theta_{\mathrm{lab}})^{\mathrm{min}}$ varies with E_α for reaction (1): the cosine is not defined below a certain

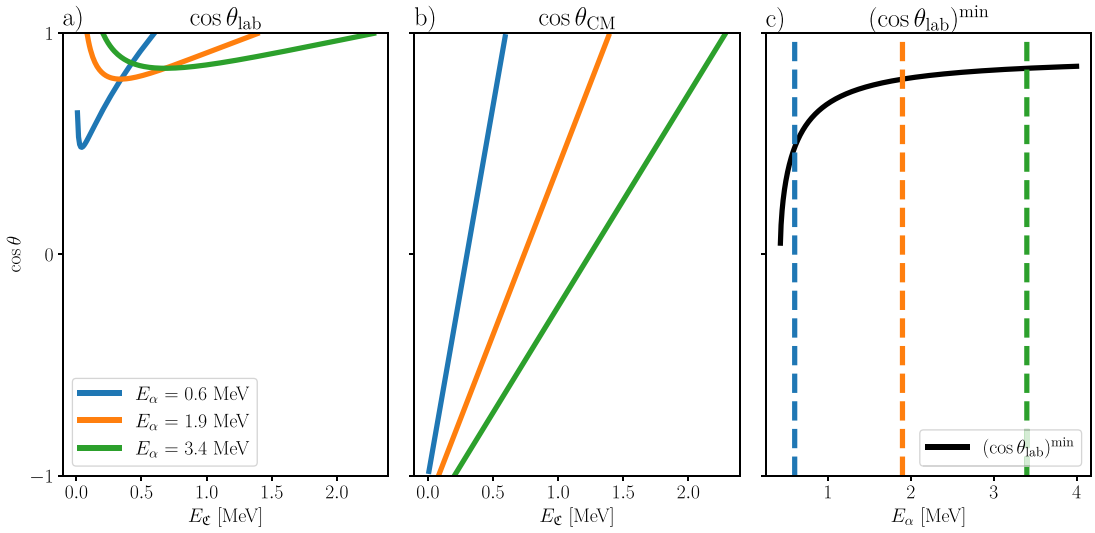

Figure 2. Emission angle cosines as a function of excited carbon energy in the laboratory (panel (*a*)) and center-of-mass (panel (*b*)) rest frames, for a fixed alpha particle energy. Panel (*c*) shows the minimum cosine of laboratory emission angle as a function of the alpha-particle energy, with the previously selected alpha particle energies in dashed vertical lines.

energy value, and it asymptotically goes to 1 for $E_\alpha \to \infty$. Using the coefficients in (10) and the definition $Q_{\rm eff} = (m_\alpha + m_{\rm Be} - m_{\mathfrak{C}} - m_{\rm n})c^2$, setting the left-hand side of equation (11) to zero gives

$$E_\alpha^{\rm thresh} = \frac{Q_{\rm eff}\left(\frac{Q_{\rm eff}}{c^2} + 2m_{\rm n}\right)}{2\left(m_{\mathfrak{C}} - m_{\rm Be}\right)} \approx 0.426\,\text{MeV}\,. \tag{12}$$

The threshold value in equation (12) is important when considered together with the cross section for the reaction. In the case of (1) for thermonuclear plasmas, it is clear from figure 3 that for slowing-down fusion-born alpha particles with $E_\alpha = 3.5\,\text{MeV}$ the reactivity $\sigma v_{\rm rel} \approx \sigma v_\alpha$ will dominate in the region $E_\alpha > 1\,\text{MeV}$ of velocity-space. Below this value, we expect the signal to be negligible and therefore assume that we always have a one-to-two mapping (degeneracy) in $E_{\mathfrak{C}}(\cos\theta_{\rm lab})$, which corresponds to a redundancy in $\cos\theta_{\rm lab}(E_{\mathfrak{C}})$, due to the $\pm$ solutions in equation (8).

2.2. Excited carbon birth-rate distribution

To generate a $\mathfrak{C}$ birth-rate distribution in energy $E_{\mathfrak{C}}$ and pitch angle $\lambda_{\mathfrak{C}}$ due to an arbitrary alpha particle distribution f_α, we can calculate the individual contribution due to a fast alpha cold ring distribution $f_{\alpha\circ}$ [45, 52]. To evaluate the single contribution due to an $f_{\alpha\circ}$, we start from the volumetric density $n_{\mathfrak{C}}$ of emitted excited carbon per unit time, in the case of arbitrary distributions for the reactants

$$\frac{{\rm d}n_{\mathfrak{C}}}{{\rm d}t} = \int \frac{{\rm d}\sigma}{{\rm d}\Omega_{\rm lab}} {\rm d}\Omega_{\rm lab} v_{\rm rel} f_\alpha\left(\boldsymbol{v}_\alpha\right) f_{\rm Be}\left(\boldsymbol{v}_{\rm Be}\right) \times {\rm d}\boldsymbol{v}_\alpha {\rm d}\boldsymbol{v}_{\rm Be}\,, \tag{13}$$

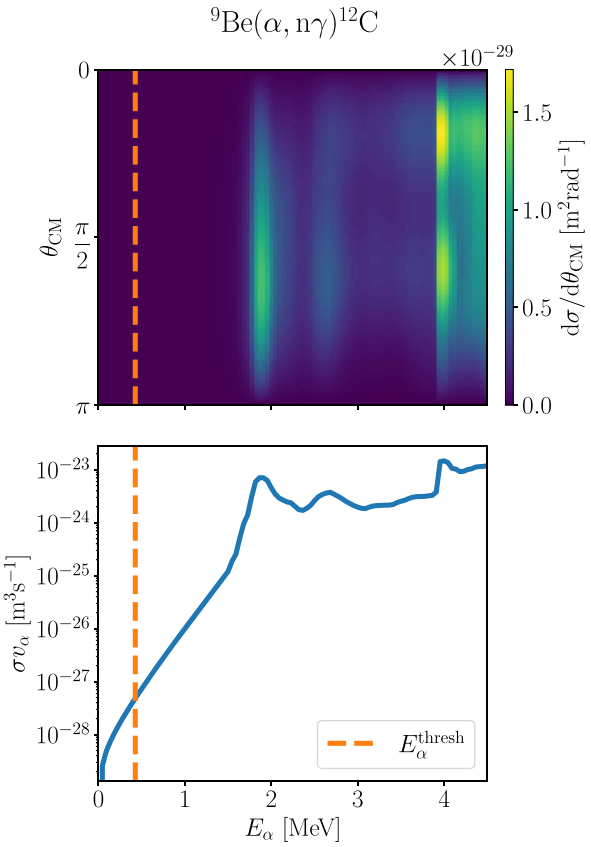

Figure 3. (Top:) differential cross section in the center-of-mass rest frame, where a bilinear spline is calculated from a patchwork of experimental data on scattered neutrons [49, 50] as done in [51]. (Bottom:) total cross section times the alpha-particle speed, which stands for the reactivity, with logarithmic scale on the *y*-axis. The kinematic threshold from equation (12) by indicated in orange dashed lines.

where $\boldsymbol{v}_s$ is the velocity for species 's', $\Omega_{\rm lab}$ is the solid angle of emission in the laboratory rest frame and $\mathrm{d}\sigma/\mathrm{d}\Omega_{\rm lab}$ is the differential cross section for the considered reaction. Each of the two differentials $\mathrm{d}\boldsymbol{v}_\alpha$ and $\mathrm{d}\boldsymbol{v}_{\rm Be}$ can be represented in spherical coordinates as $\mathrm{d}\boldsymbol{v} = v^2 \sin\lambda \,\mathrm{d}v\,\mathrm{d}\lambda\mathrm{d}\Gamma$, where λ is the pitch angle with respect to the local magnetic field $\boldsymbol{B} = B\hat{\boldsymbol{B}}$, i.e. $\cos\lambda = (\boldsymbol{v}\cdot\hat{\boldsymbol{B}})/v$ (with a minus sign if the magnetic field and the plasma current point in opposite directions); and Γ is the gyro-angle. Choosing the pitch angle over the pitch will result in a better resolution at the domain boundaries $\cos\lambda = \pm 1$, leading to better graphical results for the distributions. If the fast reactant distribution is a cold ring with fixed $(v_{\alpha\circ}, \lambda_{\alpha\circ})$

$$f_\alpha(\boldsymbol{v}_\alpha) = \frac{n_\alpha}{2\pi v_\alpha^2 \sin\lambda_\alpha}\delta(v_\alpha - v_{\alpha\circ})\,\delta(\lambda_\alpha - \lambda_{\alpha\circ})\ , \tag{14}$$

where n_α is the number density, and the second reactant is at rest, i.e.

$$f_{\rm Be}(\boldsymbol{v}_{\rm Be}) = n_{\rm Be}\delta(\boldsymbol{v}_{\rm Be})\ , \tag{15}$$

the integral in (13) simplifies considerably, and the excited carbon birth rate due to an alpha-particle cold ring becomes

$$\left(\frac{\mathrm{d}n_{\mathfrak{C}}}{\mathrm{d}t}\right)_\circ = n_\alpha n_{\rm Be}\int \frac{\mathrm{d}\sigma}{\mathrm{d}\Omega_{\rm lab}}\mathrm{d}\Omega_{\rm lab} v_{\rm rel}\frac{\delta(v_\alpha - v_{\alpha\circ})}{2\pi v_\alpha^2\sin\lambda_\alpha} \times\delta(\lambda_\alpha - \lambda_{\alpha\circ})\,\delta(\boldsymbol{v}_{\rm Be})\,\mathrm{d}\boldsymbol{v}_\alpha\mathrm{d}\boldsymbol{v}_{\rm Be}\ . \tag{16}$$

The azimuthal symmetry of the cross section [45, 53] further simplifies the calculations, and it reads

$$\frac{\mathrm{d}\sigma}{\mathrm{d}\Omega_{\rm lab}} = \frac{1}{2\pi}\frac{\mathrm{d}\sigma}{\mathrm{d}\cos\theta_{\rm lab}}\ . \tag{17}$$

After integration over v_α, λ_α and $\boldsymbol{v}_{\rm Be}$, noting that $v_{\rm rel} = v_{\alpha\circ}$ and making the cross section dependencies explicit, we obtain

$$\left(\frac{\mathrm{d}n_{\mathfrak{C}}}{\mathrm{d}t}\right)_\circ = \frac{n_\alpha n_{\rm Be}}{4\pi^2}v_{\alpha\circ}\int\frac{\mathrm{d}\sigma(v_{\alpha\circ},\lambda_{\alpha\circ},\Gamma_\alpha,\lambda_{\mathfrak{C}},\Gamma_{\mathfrak{C}})}{\mathrm{d}\cos\theta_{\rm lab}} \times\mathrm{d}\Omega_{\rm lab}\mathrm{d}\Gamma_\alpha. \tag{18}$$

Unlike standard forward models for NES and GRS [34, 45, 54, 55], we do not assume the fraction of solid angle to be a constant $\Delta\Omega_{\rm lab}$, but instead treat it as a degree of freedom. For two-step reactions, the product in the first step of (1) can be emitted anywhere, and the emission happens within the unit solid angle $\mathrm{d}\Omega_{\rm lab} = \mathrm{d}\cos\lambda_{\mathfrak{C}}\mathrm{d}\Gamma_{\mathfrak{C}}$. Substituting for $\mathrm{d}\Omega_{\rm lab}$, the integral in equation (18) becomes

$$\left(\frac{\mathrm{d}n_{\mathfrak{C}}}{\mathrm{d}t}\right)_\circ = \frac{n_\alpha n_{\rm Be}}{4\pi^2}v_{\alpha\circ}\int\frac{\mathrm{d}\sigma(v_{\alpha\circ},\lambda_{\alpha\circ},\Gamma_\alpha,\lambda_{\mathfrak{C}},\Gamma_{\mathfrak{C}})}{\mathrm{d}\cos\theta_{\rm lab}} \times\mathrm{d}\cos\lambda_{\mathfrak{C}}\mathrm{d}\Gamma_{\mathfrak{C}}\mathrm{d}\Gamma_\alpha\ . \tag{19}$$

We are interested in the rate per unit energy $\mathrm{d}E_{\mathfrak{C}}$ and unit pitch angle $\mathrm{d}\lambda_{\mathfrak{C}}$. We choose to first take the derivative of both sides with respect to $\lambda_{\mathfrak{C}}$, obtaining

$$\left(\frac{\mathrm{d}^2 n_{\mathfrak{C}}}{\mathrm{d}\lambda_{\mathfrak{C}}\,\mathrm{d}t}\right)_\circ = \frac{n_\alpha n_{\rm Be}}{4\pi^2}v_{\alpha\circ}\sin\lambda_{\mathfrak{C}} \times\int_{-\pi}^{\pi}\int_{-\pi}^{\pi}\frac{\mathrm{d}\sigma(v_{\alpha\circ},\lambda_{\alpha\circ},\Gamma_\alpha,\lambda_{\mathfrak{C}},\Gamma_{\mathfrak{C}})}{\mathrm{d}\cos\theta_{\rm lab}}\mathrm{d}\Gamma_{\mathfrak{C}}\mathrm{d}\Gamma_\alpha, \tag{20}$$

with $\lambda_{\mathfrak{C}}\in[0,\pi]$ and $|\mathrm{d}\cos\lambda_{\mathfrak{C}}/\mathrm{d}\lambda_{\mathfrak{C}}| = \sin\lambda_{\mathfrak{C}}$ which is always non-negative.

In a beam-target reaction, the cross section describes the probability density of emitting the excited nucleus at a certain angle $\theta_{\rm lab}$ with respect to the beam velocity (here $\boldsymbol{v}_\alpha$). The velocities in cylindrical coordinates $(\hat{\boldsymbol{b}}, \hat{\boldsymbol{e}}_{\perp 1}, \hat{\boldsymbol{e}}_{\perp 2})$ are represented as

$$\mathbf{v} \equiv \begin{pmatrix} v\cos\lambda \\ v\sin\lambda\cos\Gamma \\ v\sin\lambda\sin\Gamma \end{pmatrix} \tag{21}$$

such that, if we want to derive the cosine of the emission angle, we proceed as follows

$$\begin{aligned}\cos\theta_{\rm lab} = \hat{\boldsymbol{v}}_\alpha\cdot\hat{\boldsymbol{v}}_{\mathfrak{C}} &= \cos\lambda_\alpha\cdot\cos\lambda_{\mathfrak{C}} + \sin\lambda_\alpha\cos\Gamma_\alpha \\ &\quad\cdot\sin\lambda_{\mathfrak{C}}\cos\Gamma_{\mathfrak{C}} + \sin\lambda_\alpha\sin\Gamma_\alpha\cdot\sin\lambda_{\mathfrak{C}}\sin\Gamma_{\mathfrak{C}} \\ &= \cos\lambda_\alpha\cos\lambda_{\mathfrak{C}} + \sin\lambda_\alpha\sin\lambda_{\mathfrak{C}}\cos(\Gamma_\alpha - \Gamma_{\mathfrak{C}})\ .\end{aligned} \tag{22}$$

Equation (22) also explains the parametrization of the angular part of the cross section appearing in (18). We note that $\cos\theta_{\rm lab}$ depends only on the difference between the gyro-angles of the fast alpha and the excited carbon $\Gamma_\alpha - \Gamma_{\mathfrak{C}}$. Changing the integration variable to $\Psi = \Gamma_\alpha - \Gamma_{\mathfrak{C}}$, which we substitute for $\Gamma_{\mathfrak{C}}$, the integral in equation (20) becomes

$$\left(\frac{\mathrm{d}^2 n_{\mathfrak{C}}}{\mathrm{d}\lambda_{\mathfrak{C}}\,\mathrm{d}t}\right)_\circ = \frac{n_\alpha n_{\rm Be}}{4\pi^2}v_{\alpha\circ}\sin\lambda_{\mathfrak{C}} \times\int_{-\pi}^{\pi}\int_{-\pi+\Gamma_\alpha}^{\pi+\Gamma_\alpha}\frac{\mathrm{d}\sigma(v_{\alpha\circ},\lambda_{\alpha\circ},\lambda_{\mathfrak{C}},\Psi)}{\mathrm{d}\cos\theta_{\rm lab}}\mathrm{d}\Psi\,\mathrm{d}\Gamma_\alpha\ , \tag{23}$$

where now the integrand is a periodic function of Ψ and the integration limits are shifted by an amount Γ_α. Due to periodicity, the choice for Γ_α in the integration limits is arbitrary, and hence we can effect the integral over Γ_α, obtaining

$$\left(\frac{\mathrm{d}^2 n_{\mathfrak{C}}}{\mathrm{d}\lambda_{\mathfrak{C}}\,\mathrm{d}t}\right)_\circ = \frac{n_\alpha n_{\rm Be}}{2\pi}v_{\alpha\circ}\sin\lambda_{\mathfrak{C}}\int_{-\pi}^{\pi}\frac{\mathrm{d}\sigma(v_{\alpha\circ},\lambda_{\alpha\circ},\lambda_{\mathfrak{C}},\Psi)}{\mathrm{d}\cos\theta_{\rm lab}} \times\mathrm{d}\Psi\,, \tag{24}$$

where Γ_α and $\Gamma_{\mathfrak{C}}$ no longer appear, but only their difference Ψ. Physically, as depicted in figure 4, the excited carbon inherits the gyro-symmetry of the fast alpha particle, and hence we can assume that $\Gamma_{\mathfrak{C}}$ is also uniformly distributed in its domain $[-\pi,\pi]$.

The volumetric rate per unit energy and unit pitch angle is obtained by taking the derivative of equation (24) with respect to the energy of the excited carbon $E_{\mathfrak{C}}$. We can do this if the mapping $E_{\mathfrak{C}}(\Psi)$ is such that the resulting Jacobian $|\mathrm{d}\Psi/\mathrm{d}E_{\mathfrak{C}}|$

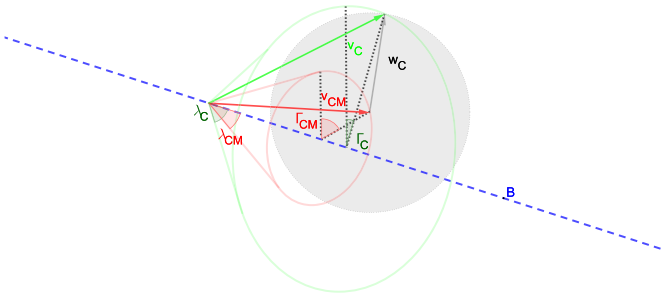

Figure 4. Schematics of double-cone symmetry. Due to the fast alpha gyration, the center-of-mass velocity rotates about the magnetic field, tracing a cone (in red). At the same time, the carbon is emitted and traces a sphere in the center-of-mass rest frame (in gray): as this happens at any point during the center-of-mass gyration (red cone), the carbon itself traces a cone of velocities (in green) which inherits uniformity in the gyro-phase.

is well defined, which requires a domain restriction to make the mapping bijective. Additionally, the chain rule needs to be applied carefully because of the degeneracy we highlighted in section 2.1. For $\Psi \in [-\pi, \pi]$, the same $\cos\theta_{\rm lab}$ values occur twice (see equation (22)) and hence we compute only one half of the integral and multiply the result by two to account for the other identical half of the integral:

$$\left(\frac{\mathrm{d}^2 n_{\mathfrak{C}}}{\mathrm{d}\lambda_{\mathfrak{C}}\,\mathrm{d}t}\right)_{\circ} = \frac{n_\alpha n_{\rm Be}}{\pi} v_{\alpha\circ} \sin\lambda_{\mathfrak{C}} \int_0^{\pi} \frac{\mathrm{d}\sigma\left(v_{\alpha\circ}, \lambda_{\alpha\circ}, \lambda_{\mathfrak{C}}, \Psi\right)}{\mathrm{d}\cos\theta_{\rm lab}} \times \mathrm{d}\Psi \,. \tag{25}$$

Now that bijectivity for $\cos\theta_{\rm lab}(\Psi)$ is ensured, we perform a change of variable in the integral such that

$$\left(\frac{\mathrm{d}^2 n_{\mathfrak{C}}}{\mathrm{d}\lambda_{\mathfrak{C}}\,\mathrm{d}t}\right)_{\circ} = \frac{n_\alpha n_{\rm Be}}{\pi} v_{\alpha\circ} \sin\lambda_{\mathfrak{C}} \times \int_{\cos\theta_{\rm lab}(\Psi=0)}^{\cos\theta_{\rm lab}(\Psi=\pi)} \frac{\mathrm{d}\sigma\left(v_{\alpha\circ}, \lambda_{\alpha\circ}, \lambda_{\mathfrak{C}}, \Psi\right)}{\mathrm{d}\cos\theta_{\rm lab}} \left|\frac{\mathrm{d}\Psi}{\mathrm{d}\cos\theta_{\rm lab}}\right| \mathrm{d}\cos\theta_{\rm lab}. \tag{26}$$

By taking the derivative of equation (26) with respect to the product energy $E_{\mathfrak{C}}$, we would obtain the following Jacobian

$$\left|\frac{\mathrm{d}\cos\theta_{\rm lab}}{\mathrm{d}E_{\mathfrak{C}}}\right|_{\pm} = \left|\frac{\mathrm{d}E_{\mathfrak{C}}}{\mathrm{d}\cos\theta_{\rm lab}}\right|_{\pm}^{-1}, \tag{27}$$

which, however, cannot be used directly (but rather, its inverse) due to the degeneracy in the mapping we highlighted at the end of section 2.1. The '−' solution is used where the product energy is below the threshold value, i.e. $E_{\mathfrak{C}} < -\mathfrak{b}/2\mathfrak{a}$, and the '+' solution if it is above, i.e. $E_{\mathfrak{C}} > -\mathfrak{b}/2\mathfrak{a}$; $E_{\mathfrak{C}} = -\mathfrak{b}/2\mathfrak{a}$ corresponds to an emission at an angle that satisfies equation (11).

We can now continue by taking the derivative of equation (26) with respect to the product energy, obtaining an analytical formula for the excited carbon volumetric rate per unit energy and unit pitch angle generated by one fast-alpha cold ring via reaction (1)

$$\left(\frac{\mathrm{d}^3 n_{\mathfrak{C}}}{\mathrm{d}E_{\mathfrak{C}}\,\mathrm{d}\lambda_{\mathfrak{C}}\,\mathrm{d}t}\right)_{\circ} = \frac{n_\alpha n_{\rm Be}}{\pi} v_{\alpha\circ} \sin\lambda_{\mathfrak{C}} \frac{\mathrm{d}\sigma\left(v_{\alpha\circ}, \lambda_{\alpha\circ}, \lambda_{\mathfrak{C}}, \Psi\right)}{\mathrm{d}\cos\theta_{\rm lab}} \times \left|\frac{\mathrm{d}\Psi}{\mathrm{d}\cos\theta_{\rm lab}}\right| \left|\frac{\mathrm{d}E_{\mathfrak{C}}}{\mathrm{d}\cos\theta_{\rm lab}}\right|_{\pm}^{-1}, \tag{28}$$

which, noting that the first Jacobian is obtained from equation (22) as $|\mathrm{d}\Psi/\mathrm{d}\cos\theta_{\rm lab}| = 1/|\sin\Psi \sin\lambda_\alpha \sin\lambda_{\mathfrak{C}}|$, we can rewrite as

$$\left(\frac{\mathrm{d}^3 n_{\mathfrak{C}}}{\mathrm{d}E_{\mathfrak{C}}\,\mathrm{d}\lambda_{\mathfrak{C}}\,\mathrm{d}t}\right)_{\circ} = \frac{n_\alpha n_{\rm Be}}{\pi} v_{\alpha\circ} \frac{\mathrm{d}\sigma\left(v_{\alpha\circ}, \lambda_{\alpha\circ}, \lambda_{\mathfrak{C}}, \Psi\right)}{\mathrm{d}\cos\theta_{\rm lab}} \times \left|\frac{1}{\sin\Psi \sin\lambda_\alpha}\right| \left|\frac{\mathrm{d}E_{\mathfrak{C}}}{\mathrm{d}\cos\theta_{\rm lab}}\right|_{\pm}^{-1}. \tag{29}$$

The differential cross section, however, is usually provided in the center-of-mass rest frame and hence includes a Jacobian describing the emission angle transformation

$$\frac{\mathrm{d}\sigma\left(v_{\alpha\circ}, \lambda_{\alpha\circ}, \lambda_{\mathfrak{C}}, \Psi\right)}{\mathrm{d}\cos\theta_{\rm lab}} = \frac{\mathrm{d}\sigma\left(v_{\alpha\circ}, \lambda_{\alpha\circ}, \lambda_{\mathfrak{C}}, \Psi\right)}{\mathrm{d}\cos\theta_{\rm CM}} \frac{\mathrm{d}\cos\theta_{\rm CM}}{\mathrm{d}\cos\theta_{\rm lab}}. \tag{30}$$

The frame-change Jacobian reads [44–46]

$$\frac{\mathrm{d}\cos\theta_{\rm CM}}{\mathrm{d}\cos\theta_{\rm lab}} = \frac{\gamma_{\rm CM}^{-2}\left[1 - \frac{v_{\rm CM}}{v_{\mathfrak{C}}}\cos\theta_{\rm lab} + \frac{v_{\rm CM}}{v_{\mathfrak{C}}^2}\left(1-\cos^2\theta_{\rm lab}\right)\frac{\mathrm{d}v_{\mathfrak{C}}}{\mathrm{d}\cos\theta_{\rm lab}}\right]}{\left[\left(1-\frac{1}{\gamma_{\rm CM}^2}\right)\cos^2\theta_{\rm lab} - 2\frac{v_{\rm CM}}{v_{\mathfrak{C}}}\cos\theta_{\rm lab} + \frac{v_{\rm CM}^2}{v_{\mathfrak{C}}^2} + \frac{1}{\gamma_{\rm CM}^2}\right]^{\frac{3}{2}}} \tag{31}$$

where $v_{\rm CM} = \gamma_\alpha m_\alpha v_\alpha/(\gamma_\alpha m_\alpha + m_{\rm Be})$ when the target beryllium-9 is stationary and $\gamma_{\rm CM} = (1 - v_{\rm CM}^2/c^2)^{-1/2}$. The derivative in the numerator of equation (31) can be obtained by the chain rule

$$\frac{\mathrm{d}v_{\mathfrak{C}}}{\mathrm{d}\cos\theta_{\rm lab}} = \frac{\mathrm{d}v_{\mathfrak{C}}}{\mathrm{d}E_{\mathfrak{C}}}\frac{\mathrm{d}E_{\mathfrak{C}}}{\mathrm{d}\cos\theta_{\rm lab}} = \frac{1}{m_{\mathfrak{C}} c \cdot \gamma_{\mathfrak{C}}^2\sqrt{\gamma_{\mathfrak{C}}^2 - 1}} \left.\frac{\mathrm{d}E_{\mathfrak{C}}}{\mathrm{d}\cos\theta_{\rm lab}}\right|_{\pm}, \tag{32}$$

where the $\pm$ reflects the two different solutions due to energy and momentum conservation. To obtain the last derivative in equation (32), we use equation (8) and obtain

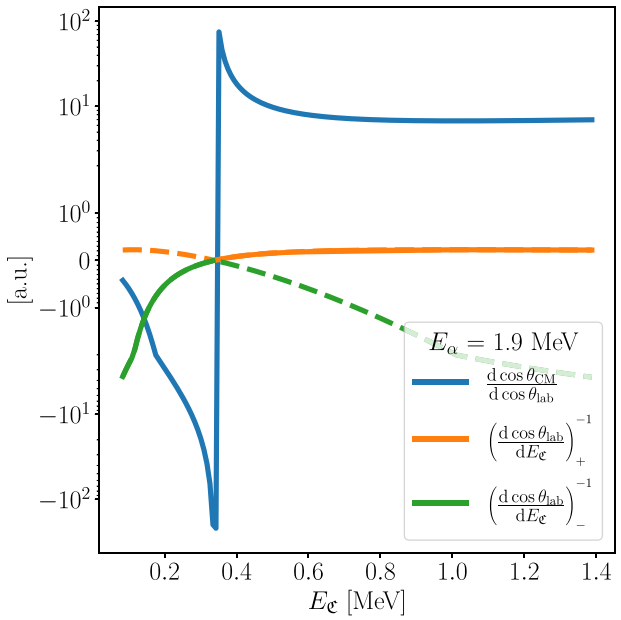

Figure 5. Derivatives from equation (29) for the Jacobians describing the transformation of the emission angle through the change of rest frame (blue) and the mapping between emission angle and product energy (orange for + solutions, green for − solutions). The scale on the y-axis is symmetric-logarithmic. The dashed lines indicate where the solutions are discarded as non physical.

$$\begin{aligned}\left.\frac{\mathrm{d}E_{\mathfrak{C}}}{\mathrm{d}\cos\theta_{\mathrm{lab}}}\right|_{\pm} &= \frac{E_\alpha c^2\left(2m_\alpha c^2+E_\alpha\right)\cos\theta_{\mathrm{lab}}}{2\left(A^2c^4-E_\alpha\left(2m_\alpha c^2+E_\alpha\right)\cos\theta^2_{\mathrm{lab}}\right)^2}\\ &\times\frac{1}{\sqrt{E_\alpha\left(2m_\alpha c^2+E_\alpha\right)\cos\theta^2_{\mathrm{lab}}}}\\ &\times\frac{1}{\sqrt{\left(4m^2_{\mathfrak{C}}\left(E_\alpha\left(2m_\alpha c^2+E_\alpha\right)\cos\theta^2_{\mathrm{lab}}-A^2c^4\right)+B^2\right)}}\\ &\times\Bigg(-4A^4m^2_{\mathfrak{C}}c^8+A^2c^4(B^2+4E_\alpha m^2_{\mathfrak{C}}(2c^2m_\alpha+E_\alpha)\\ &\quad\times\cos\theta^2_{\mathrm{lab}})\pm 2ABc^2\sqrt{E_\alpha\left(2m_\alpha c^2+E_\alpha\right)\cos\theta^2_{\mathrm{lab}}}\\ &\quad\times\sqrt{\left(4m^2_{\mathfrak{C}}\left(E_\alpha\left(2m_\alpha c^2+E_\alpha\right)\cos\theta^2_{\mathrm{lab}}-A^2c^4\right)+B^2\right)}\\ &\quad+B^2E_\alpha\left(2m_\alpha c^2+E_\alpha\right)\cos\theta^2_{\mathrm{lab}}\Bigg)\end{aligned}\tag{33}$$

where A and B are given in equation (10).

In figure 5 we show the Jacobians of equations (31) and (33) as a function of the product energy $E_{\mathfrak{C}}$. There exists a critical energy at which $\mathrm{d}\cos\theta_{\mathrm{CM}}/\mathrm{d}\cos\theta_{\mathrm{lab}}$ diverges and $\mathrm{d}E_{\mathfrak{C}}/\mathrm{d}\cos\theta_{\mathrm{lab}}$ goes to zero; this critical energy, in the case of two-step reactions, can be reached for fusion-relevant fast reactant energies, due to the low Q_{eff}. This energy corresponds to an emission at an angle with $(\cos\theta_{\mathrm{lab}})^{\mathrm{min}}$ given by equation (11). The singularity, however, is removable in the analytical implementation by using the chain rule. Combining the Jacobians in equation (29), i.e. the frame-change Jacobian and the last derivative,

$$\begin{aligned}\frac{\mathrm{d}\cos\theta_{\mathrm{CM}}}{\mathrm{d}\cos\theta_{\mathrm{lab}}}\cdot\left(\frac{\mathrm{d}E_{\mathfrak{C}}}{\mathrm{d}\cos\theta_{\mathrm{lab}}}\right)^{-1}_{\pm} &= \left.\frac{\mathrm{d}\cos\theta_{\mathrm{CM}}}{\mathrm{d}E_{\mathfrak{C}}}\right|_{\pm}\\ &= \frac{\left[\left(1-\frac{v_{\mathrm{CM}}}{v_{\mathfrak{C}}}\cos\theta_{\mathrm{lab}}\right)\left(\frac{\mathrm{d}E_{\mathfrak{C}}}{\mathrm{d}\cos\theta_{\mathrm{lab}}}\right)^{-1}_{\pm}+\frac{v_{\mathrm{CM}}}{v^3_{\mathfrak{C}}}\left(1-\cos^2\theta_{\mathrm{lab}}\right)\frac{\mathrm{d}v_{\mathfrak{C}}}{\mathrm{d}E_{\mathfrak{C}}}\right]}{\gamma^2_{\mathrm{CM}}\left[\left(1-\frac{1}{\gamma^2_{\mathrm{CM}}}\right)\cos^2\theta_{\mathrm{lab}}-2\frac{v_{\mathrm{CM}}}{v_{\mathfrak{C}}}\cos\theta_{\mathrm{lab}}+\frac{v^2_{\mathrm{CM}}}{v^2_{\mathfrak{C}}}+\frac{1}{\gamma^2_{\mathrm{CM}}}\right]^{\frac{3}{2}}}\end{aligned}\tag{34}$$

where the additional derivatives appearing are given in equations (33) and (32). The advantage with equation (34) is that, numerically, it can be implemented regardless of where the mathematical singularity is (which appears as artificial 'spikes' in the spectrum in the case of Monte Carlo simulations).

Finally, we highlight that the excited carbon birth-rate distribution due to an arbitrary f_α will be a linear combination of the contributions due to single $f_{\alpha\circ}$. In standard Cartesian coordinates [52], the birth-rate distribution due to an alpha cold ring with index $\circ$ can be defined as

$$\left(\frac{\mathrm{d}f_{\mathfrak{C}}}{\mathrm{d}t}\right)_{\circ}\equiv\frac{m_{\mathfrak{C}}}{2\pi\,v_{\mathfrak{C}}\sin\lambda_{\mathfrak{C}}}\times\left(\frac{\mathrm{d}^3n_{\mathfrak{C}}}{\mathrm{d}E_{\mathfrak{C}}\,\mathrm{d}\lambda_{\mathfrak{C}}\,\mathrm{d}t}\right)_{\circ},\tag{35}$$

where the prefactor is the Jacobian for the change in coordinate system from 2D cylindrical to 3D Cartesian. From this, we can conclude that

$$\begin{aligned}\frac{\mathrm{d}f_{\mathfrak{C}}}{\mathrm{d}t} = \frac{m_{\mathfrak{C}}}{2\pi\,v_{\mathfrak{C}}\sin\lambda_{\mathfrak{C}}}\sum_{\circ}\int\left(\frac{\mathrm{d}^3n_{\mathfrak{C}}}{\mathrm{d}E_{\mathfrak{C}}\,\mathrm{d}\lambda_{\mathfrak{C}}\,\mathrm{d}t}\right)_{\circ}f_{\alpha\circ}\left(\boldsymbol{x}_\alpha,\boldsymbol{v}_\alpha\right)\\ \times\mathrm{d}\boldsymbol{x}_\alpha\mathrm{d}\boldsymbol{v}_\alpha\end{aligned}\tag{36}$$

where $\boldsymbol{v}_\alpha$ is the alpha velocity and $\boldsymbol{x}_\alpha$ is the alpha position. Equation (36) is of general value, since it can be applied to any one-step reaction to calculate the birth-rate due to an arbitrary distribution of the fast reactant whenever the second reactant can be assumed at rest. This corresponds to a source term in the Fokker-Planck equation for the time evolution of a distribution function.

We show some examples for birth-rate distributions of the excited carbon originating from fast-alpha cold-ring distributions interacting with bulk (stationary) beryllium-9 in figure 6. We also study alphas above the nominal fusion-born energy $E_\alpha > 3.5$ MeV, which can appear if MeV-range deuterium or tritium are present in the plasma. The birth rate of excited carbon is maximized for $E_\alpha = 1.9$ MeV in panel (*d*) as a result of both the narrow birth profile and the cross-section peak shown in figure 3. One can note the up-down symmetry between the first row (*a*)–(*c*) and the third row (*g*)–(*i*) of panels; and additionally how the momentum of the carbon after the reaction tends to be biased towards the momentum of the alpha before the reaction. We remark that choosing the pitch-angle instead of the pitch value as a velocity coordinate results in a better resolution at the boundaries of the domain where $\cos\lambda = \pm 1$. Lastly, we note that the y-axes run from π to 0, such that the plots respect the standard representation based on the pitch; hence, $\cos\lambda = 1$ corresponds to $\lambda = 0$ and appears in the upper part of each figure.

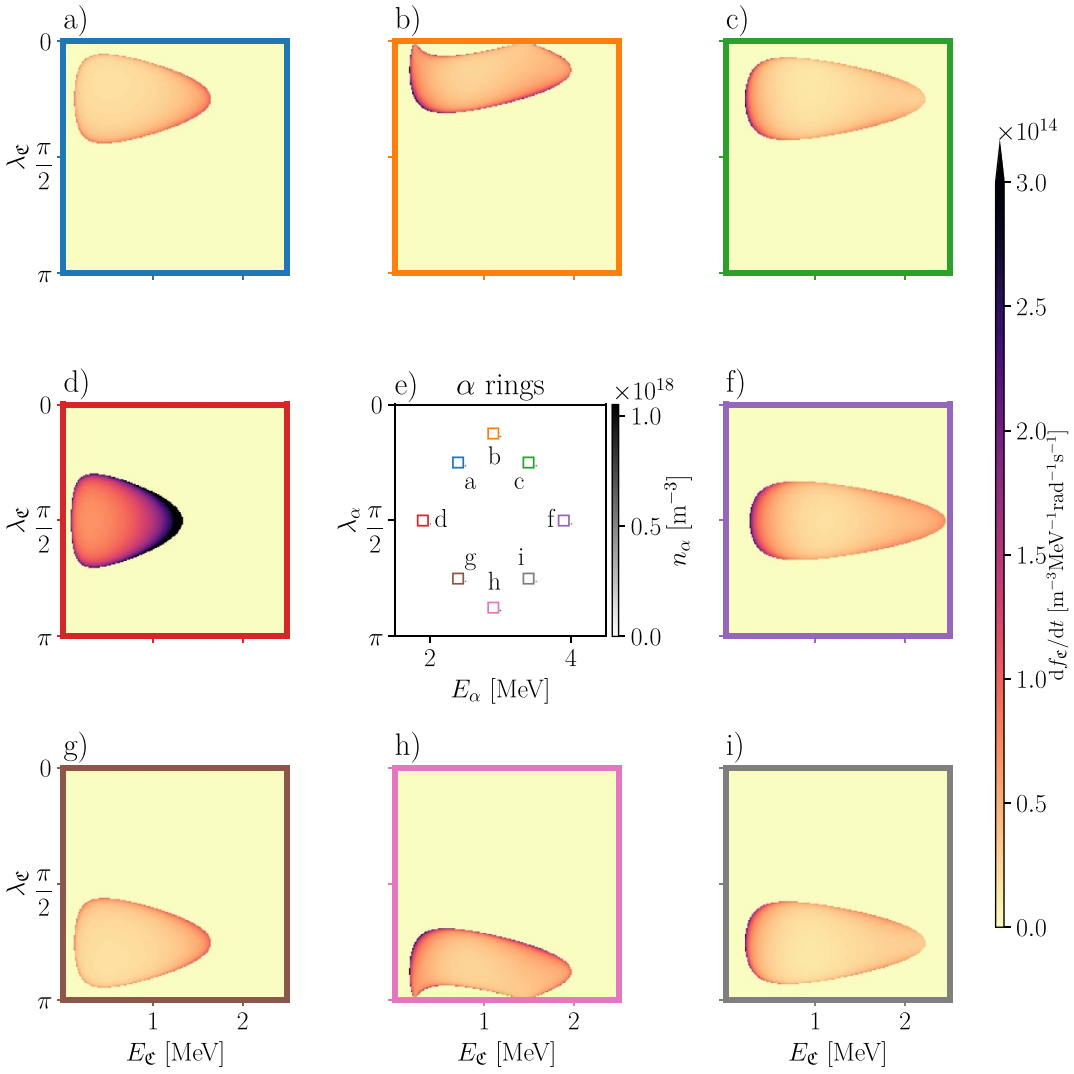

Figure 6. Energy and pitch angle scan of alpha-particle cold rings (central panel), with resulting excited carbon birth distributions in 2D velocity space (surrounding panels). A single alpha cold ring is highlighted with the same color as the corresponding 2D excited carbon distribution panel.

2.3. Decay gamma-ray spectra

Having computed the birth-rate distribution of the excited carbon, we can calculate the gamma-ray energy spectra due to a cold ring with $(E_{\mathfrak{C}}, \lambda_{\mathfrak{C}})$. The spectra will be the volumetric rate per unit gamma-ray energy d$E_{\rm g}$. The gamma-ray volumetric rate towards the detector, due to a fast alpha cold ring (with index $\circ$), will be the sum of the excited carbon cold ring contributions (with index $\circ'$) that form the birth-rate distribution $(\mathrm{d}f_{\mathfrak{C}\circ'}/\mathrm{d}t)_\circ$. This implies that

$$\left(\frac{\mathrm{d}n_{\rm g}}{\mathrm{d}t}\right)_\circ = \sum_{\circ'} \int \frac{\mathrm{d}W}{\mathrm{d}\Omega_{\rm lab}} \mathrm{d}\Omega_{\rm lab} \left(\frac{\mathrm{d}f_{\mathfrak{C}\circ'}(\boldsymbol{v}_{\mathfrak{C}})}{\mathrm{d}t}\right)_\circ \mathrm{d}\boldsymbol{v}_{\mathfrak{C}} \,, \tag{37}$$

where $\mathrm{d}\Omega_{\rm lab} = \mathrm{d}\cos\xi_{\rm lab}\mathrm{d}\psi_{\rm lab}$ is the fraction of solid angle where the gamma ray is emitted and $\mathrm{d}W/\mathrm{d}\Omega_{\rm lab}$ in sr^{-1} represents the probability density of emitting a photon g towards the detector with an angle $\xi_{\rm lab}$ with respect to the excited carbon velocity $\boldsymbol{v}_{\mathfrak{C}}$. Inserting equation (14), in the case of excited carbon, yields

$$\left(\frac{\mathrm{d}n_{\rm g}}{\mathrm{d}t}\right)_\circ = \sum_{\circ'} \int \frac{\mathrm{d}W}{\mathrm{d}\Omega_{\rm lab}} \mathrm{d}\Omega_{\rm lab} \frac{(\mathrm{d}n_{\mathfrak{C}\circ'}/\mathrm{d}t)_\circ}{2\pi v_{\mathfrak{C}}^2 \sin\lambda_{\mathfrak{C}}} \delta(v_{\mathfrak{C}} - v_{\mathfrak{C}\circ'}) \times \delta(\lambda_{\mathfrak{C}} - \lambda_{\mathfrak{C}\circ'}) \mathrm{d}\boldsymbol{v}_{\mathfrak{C}} \,, \tag{38}$$

where $(\mathrm{d}n_{\mathfrak{C}\circ'}/\mathrm{d}t)_\circ$ is the volumetric rate of excited carbon at the phase-space position with index $\circ'$ due to an alpha cold ring with index $\circ$. For high-temperature systems, we can assume the gamma-ray emission probability density to be isotropic in the rest frame of the excited carbon [56], such that there only remains a Jacobian describing the relativistic aberration of light between the source (i.e. the carbon) and the observer (i.e. the laboratory)

$$\frac{\mathrm{d}W}{\mathrm{d}\Omega_{\rm lab}} = \frac{1}{4\pi} \left|\frac{\mathrm{d}\Omega_{\mathfrak{C}}}{\mathrm{d}\Omega_{\rm lab}}\right| \,. \tag{39}$$

In equation (39), the probability of emitting a photon is biased in some direction due to the ratio of the differential emission angles on the right-hand side. This direction, contained in the expression for the Jacobian, coincides with the velocity of the source; i.e. the 'searchlight effect' described by the relativistic aberration of light [57]. Inserting this in equation (38), we obtain

$$\left(\frac{\mathrm{d}n_\mathrm{g}}{\mathrm{d}t}\right)_\circ = \frac{1}{4\pi}\sum_{\circ'}\int\left|\frac{\mathrm{d}\Omega_\mathfrak{C}}{\mathrm{d}\Omega_\mathrm{lab}}\right|\mathrm{d}\Omega_\mathrm{lab}\frac{(\mathrm{d}n_{\mathfrak{C}\circ'}/\mathrm{d}t)_\circ}{2\pi\, v_\mathfrak{C}^2\sin\lambda_\mathfrak{C}} \times\delta\left(v_\mathfrak{C}-v_{\mathfrak{C}\circ'}\right)\delta\left(\lambda_\mathfrak{C}-\lambda_{\mathfrak{C}\circ'}\right)\mathrm{d}\boldsymbol{v}_\mathfrak{C}\,. \tag{40}$$

Similarly to [45, 46], we can treat the emission angle as a constant throughout the integration, this time because the excited carbon decays on such a fast time scale [34] (∼1 ps) that we can neglect its motion right after birth. Integration over the excited carbon speed and pitch-angle gives

$$\left(\frac{\mathrm{d}n_\mathrm{g}}{\mathrm{d}t}\right)_\circ = \frac{\Delta\Omega_\mathrm{lab}}{8\pi^2}\sum_{\circ'}\left(\frac{\mathrm{d}n_{\mathfrak{C}\circ'}}{\mathrm{d}t}\right)_\circ\int_{-\pi}^{\pi}\left|\frac{\mathrm{d}\Omega_{\mathfrak{C}\circ'}}{\mathrm{d}\Omega_\mathrm{lab}}\right|\mathrm{d}\Gamma_\mathfrak{C}\,. \tag{41}$$

We can then take the derivative with respect to the gamma-ray energy E_g. Accounting for the pair of equivalent solutions in the full gyro-angle domain (to preserve bijectivity), equation (41) becomes

$$\left(\frac{\mathrm{d}^2n_\mathrm{g}}{\mathrm{d}E_\mathrm{g}\,\mathrm{d}t}\right)_\circ = \frac{\Delta\Omega_\mathrm{lab}}{4\pi^2}\sum_{\circ'}\left(\frac{\mathrm{d}n_{\mathfrak{C}\circ'}}{\mathrm{d}t}\right)_\circ\left|\frac{\mathrm{d}\Omega_{\mathfrak{C}\circ'}}{\mathrm{d}\Omega_\mathrm{lab}}\right|\left|\frac{\mathrm{d}\Gamma_{\mathfrak{C}\circ}}{\mathrm{d}E_\mathrm{g}}\right|\,. \tag{42}$$

The Jacobian that governs the emission angle transformation, as in equation (31), is obtained from relativistic velocity addition formula, where in this case the emitted particle is a photon with $v_g = c$. This gives

$$\frac{\mathrm{d}\Omega_\mathfrak{C}}{\mathrm{d}\Omega_\mathrm{lab}} = \frac{\mathrm{d}\cos\xi_\mathfrak{C}}{\mathrm{d}\cos\xi_\mathrm{lab}} = \frac{\gamma_\mathfrak{C}^{-2}\left[1-\frac{v_\mathfrak{C}}{c}\cos\xi_\mathrm{lab}\right]}{\left[\left(1-\frac{1}{\gamma_\mathfrak{C}^2}\right)\cos^2\xi_\mathrm{lab}-2\frac{v_\mathfrak{C}}{c}\cos\xi_\mathrm{lab}+\frac{v_\mathfrak{C}^2}{c^2}+\frac{1}{\gamma_\mathfrak{C}^2}\right]^{\frac{3}{2}}}. \tag{43}$$

We note that the derivative in the numerator of equation (31) does not appear here, since the speed of light is always the same regardless of the reference frame. In the first step of equation (43), we exploited the fact that the azimuthal direction is not affected by the change of rest frame [58, 59], namely:

$$\frac{\mathrm{d}\Omega_\mathfrak{C}}{\mathrm{d}\Omega_\mathrm{lab}} = \frac{\mathrm{d}\cos\xi_\mathfrak{C}\mathrm{d}\psi_\mathfrak{C}}{\mathrm{d}\cos\xi_\mathrm{lab}\mathrm{d}\psi_\mathrm{lab}} = \frac{\mathrm{d}\cos\xi_\mathfrak{C}}{\mathrm{d}\cos\xi_\mathrm{lab}} \tag{44}$$

with ξ, ψ the polar and azimuthal angles.

The second Jacobian appearing in equation (42) can be obtained from the definition of relativistic Doppler-shift caused by a moving source (in our case, the excited carbon) and measured by an observer (in our case, the detector in the laboratory rest frame). The gamma-ray energy measured by the observer is

$$E_\mathrm{g} = \frac{E_{g0}}{\gamma_\mathfrak{C}\left(1-\frac{v_\mathfrak{C}}{c}\cdot\hat{\boldsymbol{u}}_\mathrm{g}\right)}\,, \tag{45}$$

where the unit vector $\hat{\boldsymbol{u}}_\mathrm{g}$ points towards the detector along its line of sight. Once again, the emission angle is naturally contained in the calculation of the product energy (recall equation (8)) since now $\cos\xi_\mathrm{lab} \equiv \hat{\boldsymbol{v}}_\mathfrak{C}\cdot\hat{\boldsymbol{u}}_\mathrm{g}$; we can rewrite equation (45) as

$$E_\mathrm{g} = \frac{E_{g0}/\gamma_\mathfrak{C}}{1-\frac{v_\mathfrak{C}}{c}\cos\xi_\mathrm{lab}}\,. \tag{46}$$

Equation (22) suggests a relationship between emission angle ξ_lab and fast ion gyro-angle $\Gamma_\mathfrak{C}$, whenever the emission occurs exclusively along a line of sight with tilt angle ϕ with respect to the local magnetic field (once a detector geometry is chosen), and write:

$$\cos\xi_\mathrm{lab} = \cos\lambda_\mathfrak{C}\cos\phi - \sin\lambda_\mathfrak{C}\sin\phi\sin\Gamma_\mathfrak{C}\,, \tag{47}$$

from which we can obtain the second Jacobian in equation (42) by using the chain-rule:

$$\frac{\mathrm{d}\Gamma_\mathfrak{C}}{\mathrm{d}E_\mathrm{g}} = \frac{\mathrm{d}\Gamma_\mathfrak{C}}{\mathrm{d}\sin\Gamma_\mathfrak{C}}\frac{\mathrm{d}\sin\Gamma_\mathfrak{C}}{\mathrm{d}\cos\xi_\mathrm{lab}}\frac{\mathrm{d}\cos\xi_\mathrm{lab}}{\mathrm{d}E_\mathrm{g}} = \frac{1}{\cos\Gamma_\mathfrak{C}}\frac{-1}{\sin\lambda_\mathfrak{C}\sin\phi}\frac{E_{g0}}{E_\mathrm{g}^2\sqrt{\gamma_\mathfrak{C}^2-1}}\,. \tag{48}$$

We can now insert the two Jacobians in equation (42) with the cold ring index $\circ'$ attached, such that the gamma-ray energy spectrum due to an excited carbon distribution generated by a fast alpha cold ring with index $\circ$ and observed with an angle ϕ with respect to the local magnetic field is

$$\left(\frac{\mathrm{d}^2n_\mathrm{g}}{\mathrm{d}E_\mathrm{g}\,\mathrm{d}t}\right)_\circ = \frac{\Delta\Omega_\mathrm{lab}}{4\pi^2}\sum_{\circ'}\left(\frac{\mathrm{d}n_{\mathfrak{C}\circ'}}{\mathrm{d}t}\right)_\circ\left|\frac{\mathrm{d}\Omega_{\mathfrak{C}\circ'}}{\mathrm{d}\Omega_\mathrm{lab}}\right|\left|\frac{1}{\cos\Gamma_\mathfrak{C}}\right| \times\left|\frac{1}{\sin\lambda_{\mathfrak{C}\circ'}\sin\phi}\right|\left|\frac{E_{g0}}{E_\mathrm{g}^2\sqrt{\gamma_{\mathfrak{C}\circ'}^2-1}}\right|. \tag{49}$$

In figure 7 we show some examples of gamma-ray spectra generated from the combination of fast-alpha cold rings presented in figure 6, in the case of perpendicular viewing angle $\phi = 90°$ of the detector with respect to the magnetic field and of $\Delta\Omega_\mathrm{lab} = 4\pi\times10^{-3}$ sr. Notably, for alpha cold rings with supplementary angles, i.e. $\lambda_\alpha = \pi - \lambda'_\alpha$, the carbon birth distributions are mirrored about $\lambda_\alpha = \pi/2$, which then implies that the signals overlap perfectly; in the figure, we plot them as dashed lines to obviate this. This fact is explained by looking at equation (47), where one can see that for $\cos\phi = 0$ the first term on the right-hand side vanishes and hence the spectra only depend on $\sin\lambda_\mathfrak{C}$—which has the same values for mirrored distributions. Equation (47), if combined with equation (46) for the Doppler shift, also explains

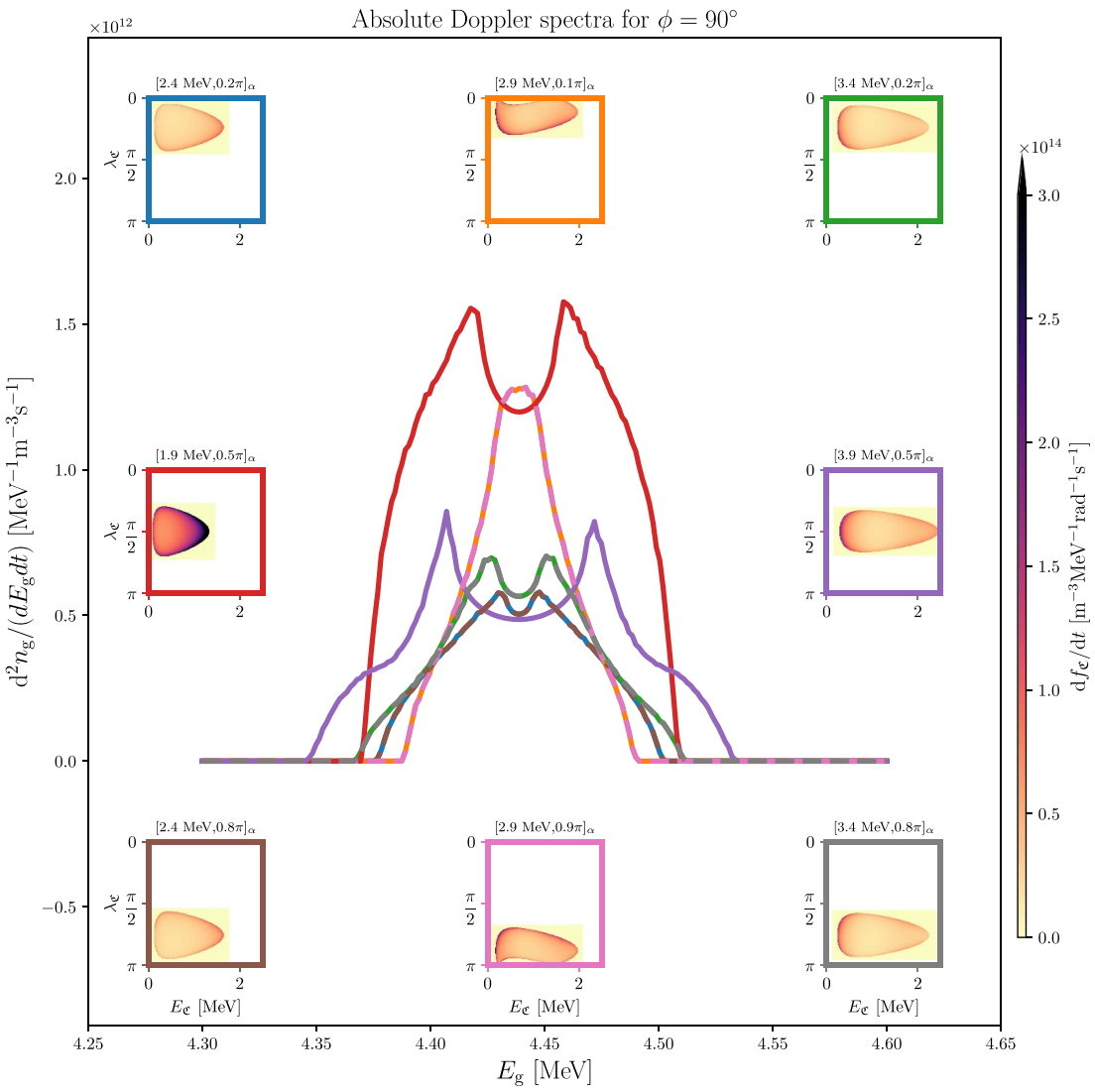

Figure 7. Gamma-ray Doppler spectra generated by the birth distributions calculated in figure 6, where the same color scheme is adopted, in the case of viewing angle $\phi = 90°$. To label each spectrum, we keep the excited carbon distributions in small color-framed plots at the edge of the panels. Exactly overlapping lines are plotted as dashed lines. The colorbar on the right-hand side refers to the excited carbon plots, as done before.

how the tails of the spectra extend towards the blue- and red-shifted sides of the spectrum: the purple colored signal extends the longest since the corresponding carbon birth distribution has the highest maximum perpendicular velocity, for example. Closer to the nominal gamma-ray energy $E_{\mathrm{g}0} \simeq 4.44\,\mathrm{MeV}$, instead, the signal is dominated by the red colored signal, due to the cross-section resonance at $E_\alpha \simeq 1.9\,\mathrm{MeV}$ increasing the birth rate of excited carbon, and by the pink-orange colored signals, due to the low projected velocity of the excited carbon along the line-of-sight (since the birth distributions are mostly squeezed toward $\lambda_\mathfrak{C} = 0$ and $\lambda_\mathfrak{C} = \pi$). Additionally, the 'double-humped' shapes observed here are in very good agreement with other simulations [34] and experiments [40] whenever detectors are able to resolve the Doppler shift accurately enough.

In figure 8, we choose two different viewing angles $\phi = 60°, 30°$ to highlight the changes in the spectra with respect to figure 7. Instead of the full excited carbon distributions that generate them, we only indicate the velocity-space coordinates of the initial fast-alpha cold ring that produced the excited carbon. The main difference, with respect to figure 7, is that supplementary alpha cold ring pitch angles do not lead to identical spectra now: the same birth distributions as before can now be distinguished by the detector since the corresponding signal is mirrored with respect to $E_{\mathrm{g}0} \simeq 4.44\,\mathrm{MeV}$. At $\phi = 30°$ (right panel), the first term in equation (47) is the largest and hence the separation between mirrored spectra (one red-shifted, one blue-shifted) is even higher. Additionally, as the projection of the perpendicular velocity is reduced (from $\phi = 90°$, to $60°$, to $30°$) the double-humped shape is less and less pronounced, until only a single peak is formed at the center of the spectrum.

3. Benchmark

In this section we provide a comparison between the model derived here and the calculations obtained by the Monte Carlo

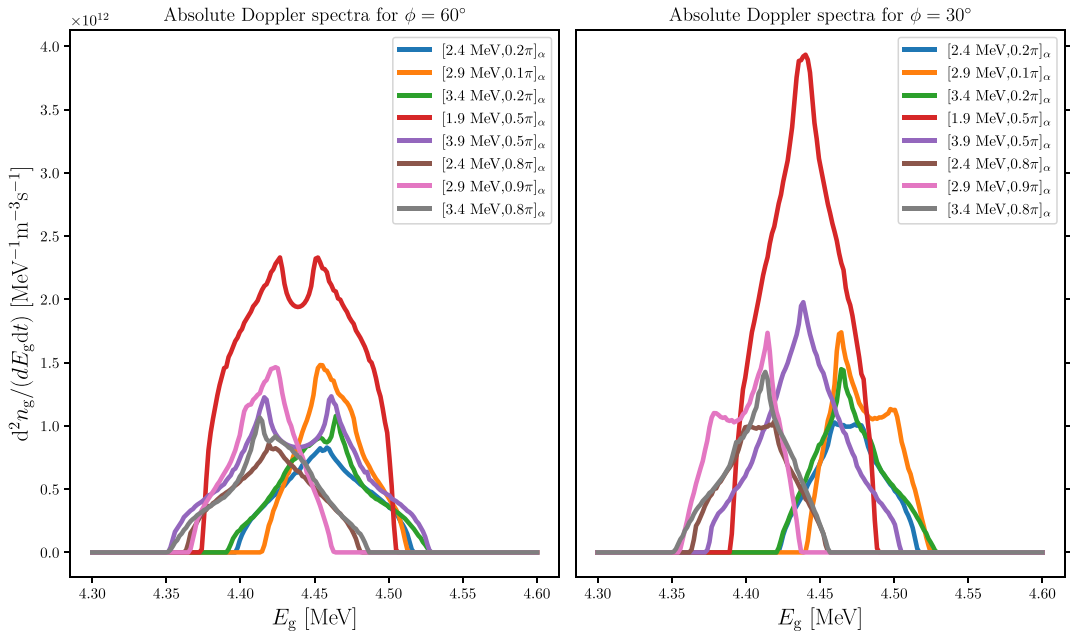

Figure 8. Gamma-ray Doppler spectra generated by the birth distributions calculated in figure 6, where the same color scheme is adopted, in the case of viewing angles $\phi = 60°$ (left panel) and $\phi = 30°$ (right panel). The legends here are substitutes for the small 2D plots in figure 7.

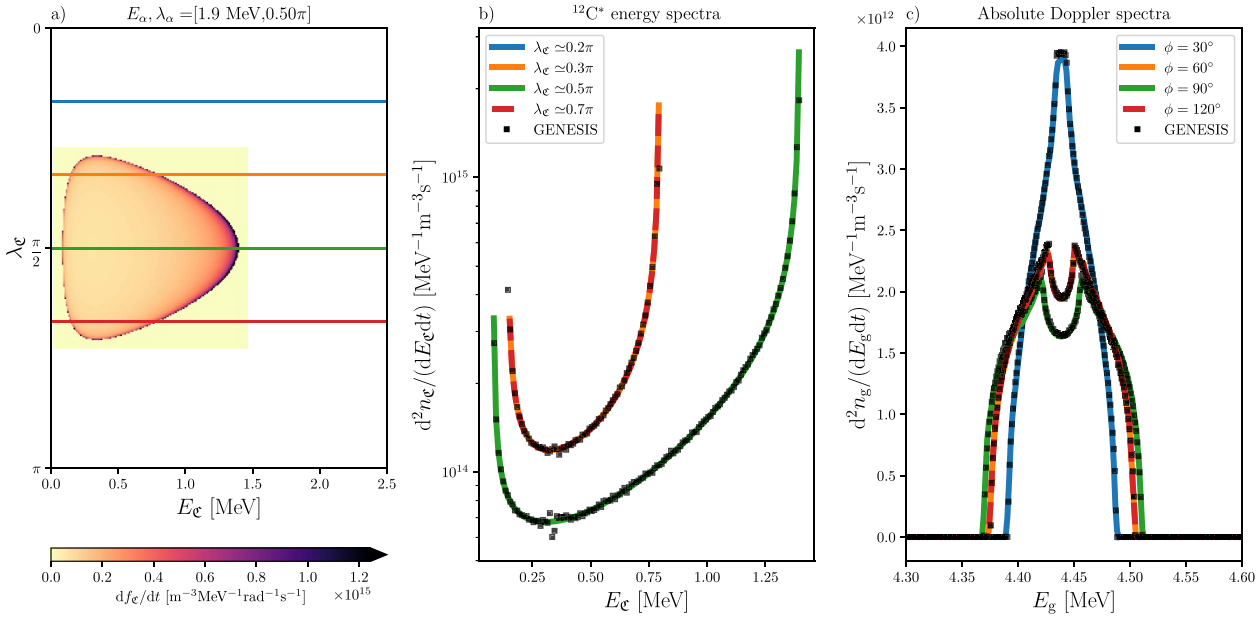

Figure 9. Panel (a) shows the excited carbon distribution due to an alpha particle cold ring with $E_\alpha = 1.9\,\mathrm{MeV}$ and $\lambda_\alpha = \pi/2$. Panel (b) shows the same distribution when compared with Monte Carlo calculations (black dots) for constant pitch-angle values (colored lines); the dashed lines are used when calculations are exactly overlapping. Panel (c) shows the gamma-ray Doppler spectra due to the distribution in panel (a) for a set of different viewing angles ϕ.

code GENESIS [34, 37]. Since we consider two-step reactions, we choose to compare both the excited carbon output and the resulting gamma-ray spectra. Since an arbitrary alpha particle distribution can be decomposed in a series of cold rings, we perform the benchmark on this elementary unit only, given that the full signal is then reconstructed by simple summation i.e.

$$\left(\frac{\mathrm{d}^2 n_\mathrm{g}}{\mathrm{d}E_\mathrm{g}\,\mathrm{d}t}\right)_\mathrm{tot} = \sum_\circ \int \left(\frac{\mathrm{d}^2 n_\mathrm{g}}{\mathrm{d}E_\mathrm{g}\,\mathrm{d}t}\right)_\circ f_{\alpha\circ}(\boldsymbol{x}_\alpha, \boldsymbol{v}_\alpha)\,\mathrm{d}\boldsymbol{x}_\alpha \mathrm{d}\boldsymbol{v}_\alpha\,. \quad (50)$$

In figure 9, we can observe the step-by-step process that leads to the spectrum formation: a single alpha-particle cold ring generates a full 2D carbon birth distribution (panel (a)). The energy distributions for different pitch-angle values $\lambda_\mathfrak{C}$ are shown in panel (b). The gamma-ray energy spectra for different viewing angles ϕ according to equation (49) are shown in panel (c). For the calculations, the only free parameters are the initial alpha particle and beryllium densities, which we set to $n_\alpha = n_\mathrm{Be} = 10^{18}\,\mathrm{m}^{-3}$, and the fraction of solid angle seen by

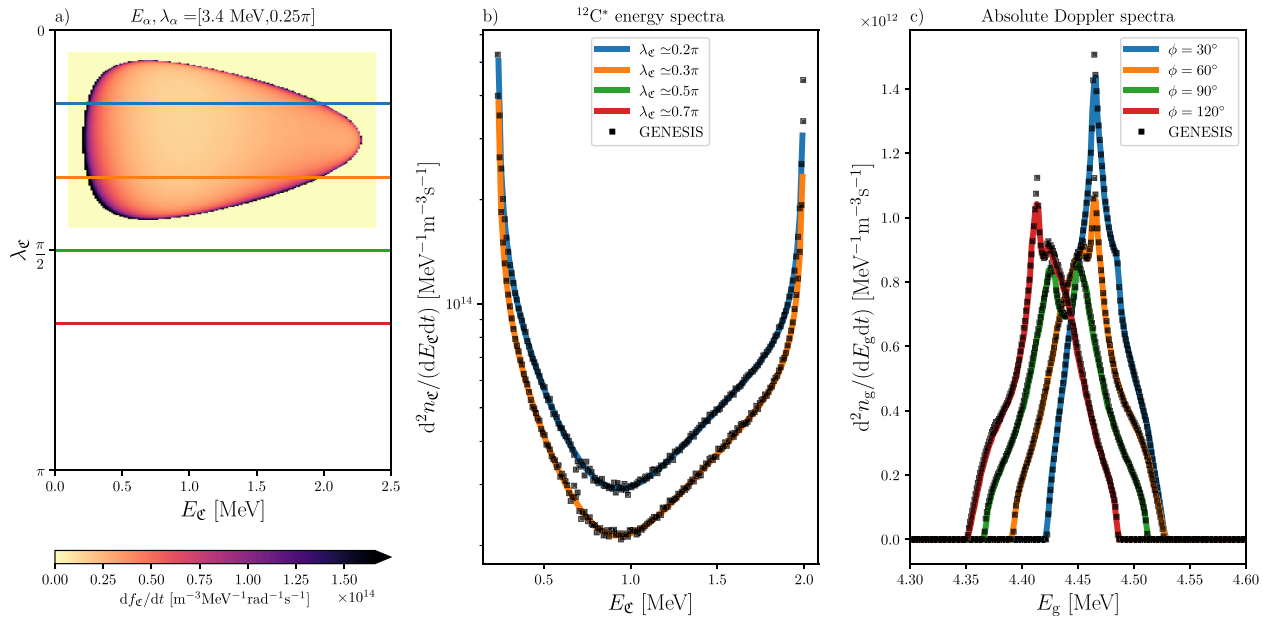

Figure 10. Panel (*a*) shows the excited carbon distribution due to an alpha particle cold ring with $E_\alpha = 3.4\,\text{MeV}$ and $\lambda_\alpha = \pi/4$. Panel (*b*) shows the same distribution when compared with Monte Carlo calculations (black dots) for constant pitch-angle values (colored lines). Panel (*c*) shows the gamma-ray Doppler spectra due to the distribution in panel (*a*) for a set of different viewing angles ϕ.

the synthetic detector, which we set to $\Delta\Omega_{\text{lab}} = 4\pi \times 10^{-3}$ sr. These values correspond to standard operational parameters for current machines; additionally, since they only linearly affect the overall scaling of the spectra, we do not explicitly show a parameter scan for densities and fraction of solid angle. Furthermore, we note that the spectrum normalization is, neglecting detection efficiency and other nuisance parameters, exactly accurate: this is typical of Monte Carlo models, but in our analytical model we have the same level of accuracy—within the margins given by the finite resolution of the grids in velocity space. One can also observe the diverging nature of the frame-change Jacobian in equation (31) that appears as a wiggle in the central part of the energy spectra of the Monte Carlo simulation in panel (*b*).

In figure 10, we can see an analogous benchmark with a different initial cold ring. The energy distribution is plotted for the same pitch-angles $\lambda_{\mathfrak{C}}$'s as in figure 9 in panel (*b*), and the viewing angles ϕ's are the same as in figure 9 in panel (*c*). It is important to highlight that the gyro-symmetry for the excited carbon in the intermediate step is an assumption in our analytical model but it is not imposed within the Monte Carlo simulation, where the products are emitted simply isotropically in the reference frame of the carbon each time.

4. Discussion

The presented model separates the gamma-ray spectrum formation into two parts, one where the excited product is generated, and one where the gamma ray is emitted and detected. This allows a better understanding of the step-by-step process and an improvement in the computational speed for these types of problems. The first part of the model can be generalized to any two-body reaction, such that fusion birth-rate distributions can be calculated directly with no statistical sampling to be made, as suggested by equation (36). These rates can be used in larger codes to evaluate fluxes of particles impinging on some machine components (e.g. vacuum vessel tiles) or to directly compute source terms for time-evolving distribution functions. For high-dimensional problems, there may be a higher need for an analytical model to compute these quantities. For one-step reactions, the analytical model is two orders of magnitude faster than the Monte Carlo code [45, 46]. On the other hand, two-step reactions modeling is only 3–5 times faster due to the additional 2D excited-product distributions to loop over to calculate the actual gamma-ray spectra. Whenever the two parts of the model are combined, instead, one can build discrete operators that map a fast-ion distribution function to the resulting signal of a detector. These objects are called weight functions, and are especially relevant when evaluating the phase-space coverage of a diagnostic setup and when performing tomographic inversion of measurements. Even in this case, solving these problems in 3D spaces (such as constants-of-motion or orbit phase spaces) can be computationally very heavy [60] if statistical sampling is needed. Future work is aimed at extending this analytical model to 3D phase spaces [36, 61–63]. By formulating this forward model in a discrete way, it is also possible to combine the information of products generated from the same reaction when solving inference problems—which might prove useful for fast-ion tomography problems.

The future of reactor-scale fusion facilities seems to be directed towards full-tungsten wall machines, where low-Z impurities such as beryllium are not expected to be present; in this case, a potentially good substitute reaction could be $^{10}B(\alpha,pg)^{13}C$, which can be triggered by injected boron and

has three distinct gamma-ray lines that could in principle be used simultaneously. While the production of three gamma-ray lines suggests that this reaction may offer enhanced alpha particle velocity space resolution, a detailed evaluation of its alpha-particle phase-space sensitivity requires knowledge of the reaction differential cross section as a function of the energy, which is currently being evaluated [64]. Results will be reported in a future publication, after data on the differential cross section are made publicly available.

5. Conclusions

This work presents an extension of an existing model that aims at calculating fusion product spectra analytically for beam-target reactions where the target reactant is at rest; now it is possible to apply it to two-step gamma-ray reactions. The calculated spectra are in very good agreement with Monte Carlo predictions, and offer much faster computation times at the expense of neglecting the dynamics of the second reactant. For the case of fusion-born alphas reacting with thermal impurities, this assumption is very well justified. This extension additionally makes it possible to calculate full 2D birth distributions of any product generated by any two-body fusion reaction, which may prove useful for other codes dealing with computationally heavy tasks.

Acknowledgments

This work has been carried out within the framework of the EUROfusion Consortium, funded by the European Union via the Euratom Research and Training Programme (Grant Agreement No. 101052200—EUROfusion). Views and opinions expressed are however those of the author(s) only and do not necessarily reflect those of the European Union or the European Commission. Neither the European Union nor the European Commission can be held responsible for them. A.V. is also supported by the 'Grants in Aid of Research' initiative from Sigma Xi, to which we are grateful for the financial support via Grant No. G20240315-8377.

ORCID iDs

A. Valentini https://orcid.org/0009-0003-5394-4267
B.C.G. Reman https://orcid.org/0000-0003-3507-9444
J. Eriksson https://orcid.org/0000-0002-0892-3358
H. Järleblad https://orcid.org/0000-0003-1126-686X
M. Rud https://orcid.org/0000-0003-2482-4461
M. Salewski https://orcid.org/0000-0002-3699-679X

References

[1] Heidbrink W.W. 2008 *Phys. Plasmas* **15** 055501
[2] Pinches S.D. 1996 Nonlinear interaction of fast particles with Alfvén waves in tokamaks *PhD Thesis* University of Nottingham
[3] Mazzi S. *et al* 2022 *Nat. Phys.* **18** 776–82
[4] Heidbrink W.W. and White R.B. 2020 *Phys. Plasmas* **27** 030901
[5] Gorelenkov N.N., Pinches S.D. and Toi K. 2014 *Nucl. Fusion* **54** 125001
[6] Pinches S.D., Chapman I.T., Lauber P.W., Oliver H.J.C., Sharapov S.E., Shinohara K. and Tani K. 2015 *Phys. Plasmas* **22** 021807
[7] Kazakov Y.O. *et al* 2017 *Nat. Phys.* **13** 973–8
[8] Kazakov Y.O. *et al* 2021 *Phys. Plasmas* **28** 020501
[9] Weiland M., Bilato R., Dux R., Geiger B., Lebschy A., Felici F., Fischer R., Rittich D. and van Zeeland M. 2018 *Nucl. Fusion* **58** 082032
[10] Van Eester D. and Lerche E. 2011 *Plasma Phys. Control. Fusion* **53** 092001
[11] Hirvijoki E., Asunta O., Koskela T., Kurki-Suonio T., Miettunen J., Sipilä S., Snicker A. and Äkäslompolo S. 2014 *Comput. Phys. Commun.* **185** 1310–21
[12] Pankin A., McCune D., Andre R., Bateman G. and Kritz A. 2004 *Comput. Phys. Commun.* **159** 157–84
[13] Moseev D., Salewski M., Garcia-Muñoz M., Geiger B. and Nocente M. 2018 *Rev. Mod. Plasma Phys.* **2** 7
[14] Heidbrink W.W., Luo Y., Burrell K.H., Harvey R.W., Pinsker R.I. and Ruskov E. 2007 *Plasma Phys. Control. Fusion* **49** 1457–75
[15] Salewski M. *et al* 2011 *Nucl. Fusion* **51** 083014
[16] Salewski M. *et al* 2014 *Plasma Phys. Control. Fusion* **56** 105005
[17] Salewski M. *et al* 2015 *Nucl. Fusion* **55** 093029
[18] Salewski M. *et al* 2016 *Nucl. Fusion* **56** 046009
[19] Jacobsen A.S., Salewski M., Eriksson J., Ericsson G., Korsholm S.B., Leipold F., Nielsen S.K., Rasmussen J. and Stejner M. 2015 *Nucl. Fusion* **55** 053013
[20] Jacobsen A.S., Binda F., Cazzaniga C., Eriksson J., Hjalmarsson A., Nocente M., Salewski M. and Tardini G. 2017 *Rev. Sci. Instrum.* **88** 073506
[21] Heidbrink W.W., Garcia A., Boeglin W. and Salewski M. 2021 *Plasma Phys. Control. Fusion* **63** 055008
[22] Rueda-Rueda J., Garcia-Munoz M., Viezzer E., Schneider P.A., Oyola P., Galdon-Quiroga J., Salewski M., Schmidt B.S. and Garcia-Dominguez J. 2024 *Plasma Phys. Control. Fusion* **66** 065025
[23] Schmidt B.S. *et al* 2023 *Phys. Plasmas* **30** 092109
[24] Salewski M. *et al* 2014 *Nucl. Fusion* **54** 023005
[25] Salewski M. *et al* 2016 *Nucl. Fusion* **56** 106024
[26] Rud M. *et al* 2024 *Nucl. Fusion* **64** 076018
[27] Schmidt B.S. *et al* 2023 *Nucl. Fusion* **63** 076016
[28] Salewski M. 2019 Fast-ion diagnostic in fusion plasmas by velocity-space tomography *Dr. Techn. Thesis* Technical University of Denmark
[29] Weiland M., Bilato R., Geiger B., Schneider P.A., Tardini G., Garcia-Muñoz M., Ryter F., Salewski M. and Zohm H. 2017 *Nucl. Fusion* **57** 116058
[30] Madsen B. *et al* 2020 *Plasma Phys. Control. Fusion* **62** 115019
[31] Nocente M. *et al* 2017 *Nucl. Fusion* **57** 076016
[32] Eriksson J. *et al* 2019 *Plasma Phys. Control. Fusion* **61** 014027
[33] Nocente M. *et al* 2020 *Plasma Phys. Control. Fusion* **62** 014015
[34] Nocente M. 2011 Neutron and gamma-ray emission spectroscopy as fast ion diagnostics in fusion plasmas *PhD Thesis* University of Milano Bicocca
[35] Kiptily V.G., Cecil F.E. and Medley S.S. 2006 *Plasma Phys. Control. Fusion* **48** R59–R82
[36] Järleblad H., Stagner L., Salewski M., Eriksson J., Nocente M., Rasmussen J., Stancar Z., Kazakov Y.O. and Simmendefeldt B. (JET Contributors) 2022 *Nucl. Fusion* **62** 112005
[37] Nocente M., Källne J., Salewski M., Tardocchi M. and Gorini G. 2015 *Nucl. Fusion* **55** 123009

[38] Dal Molin A. *et al* 2024 *Phys. Rev. Lett.* **133** 055102
[39] Tardocchi M. *et al* 2011 *Phys. Rev. Lett.* **107** 205002
[40] Kiptily V.G. *et al* 2024 *Nucl. Fusion* **64** 086059
[41] Nocente M. *et al* 2022 *Rev. Sci. Instrum.* **93** 093520
[42] Salewski M. *et al* 2018 *Nucl. Fusion* **58** 096019
[43] Korsholm S.B. *et al* 2022 *Rev. Sci. Instrum.* **93** 103539
[44] Eriksson J., Conroy S., Andersson Sundén E. and Hellesen C. 2016 *Comput. Phys. Commun.* **199** 40–46
[45] Valentini A. *et al* 2024 *Nucl. Fusion* **65** 026001
[46] Valentini A., Reman B.C.G., Nocente M., Eriksson J., Järleblad H., Moseev D., Rud M., Snicker A. and Salewski M. 2024 *Rev. Sci. Instrum.* **95** 083551
[47] Van der Zwan L. and Geiger K.W. 1970 *Nucl. Phys.* A **152** 481–94
[48] Geiger K.W. and Van Der Zwan L. 1975 *Nucl. Instrum. Methods* **131** 315–21
[49] Kiptily V.G. *et al* 1992 *Bull. Russ. Acad. Sci. Phys.* **56** 481–94
[50] Van der Zwan L. and Geiger K. 1970 *Nucl. Phys.* A **152** 481–94
[51] Nocente M. *et al* 2012 *Nucl. Fusion* **52** 063009
[52] Moseev D. and Salewski M. 2019 *Phys. Plasmas* **26** 020901
[53] Goldhaber M. and Fowler R.H. 1934 *Proc. Cambridge Phil. Soc.* **30** 561
[54] Eriksson J. 2010 Calculations of neutron energy spectra from fast ion reactions in tokamak fusion plasmas *Master's Thesis* Uppsala Universitet
[55] Bernstein M.J. and Comisar G.G. 1972 *Phys. Fluids* **15** 700–7
[56] Krane K.S. 1988 *Introductory Nuclear Physics* (Wiley) (available at: https://cds.cern.ch/record/359790)
[57] Sherin Z.W., Cheu R., Tan P. and Kortemeyer G. 2016 *Am. J. Phys.* **84** 369–74
[58] Catchen G.L., Husain J. and Zare R.N. 1978 *J. Chem. Phys.* **69** 1737–41
[59] Johnson M.H. and Teller E. 1982 *Proc. Natl Acad. Sci.* **79** 1340
[60] Järleblad H., Stagner L., Salewski M., Eriksson J., Nocente M., Schmidt B.S. and Rud Larsen M. 2024 *Comput. Phys. Commun.* **294** 108930
[61] Stagner L., Heidbrink W.W., Salewski M., Jacobsen A.S. and Geiger B. (the DIII-D and ASDEX Upgrade Teams) 2022 *Nucl. Fusion* **62** 026033
[62] Rud M. *et al* 2024 *Nucl. Fusion* **64** 036007
[63] Järleblad H., Stagner L., Salewski M., Eriksson J., Benjamin S., Madsen B., Nocente M., Rasmussen J. and Schmidt B.S. 2021 *Rev. Sci. Instrum.* **92** 043526
[64] Kiptily V. 2025 *Fusion Eng. Des.* **215** 114959